Ultrasound in Med. & Biol., Vol. 48, No. 9, pp. 1745–1761, 2022

0301-5629/$ - see front matter

https://doi.org/10.1016/j.ultrasmedbio.2022.05.001

● *Original Contribution*

TRADITIONAL MULTIWELL PLATES AND PETRI DISHES LIMIT THE EVALUATION OF THE EFFECTS OF ULTRASOUND ON CELLS *IN VITRO*

Dhanak Gupta,* Jill Savva,† Xuan Li,† James H. Chandler,‡ Richard M. Shelton,* Ben A. Scheven,* Helen Mulvana,§ Pietro Valdastri,‡ Margaret Lucas,† and A. Damien Walmsley*

* School of Dentistry, University of Birmingham, Birmingham, UK; † Centre for Medical & Industrial Ultrasonics, James Watt School of Engineering, University of Glasgow, Glasgow, UK; ‡ Science and Technology of Robotics in Medicine (STORM) Laboratory UK, School of Electronic and Electrical Engineering, University of Leeds, Leeds, UK; and § Department of Biomedical Engineering, University of Strathclyde, Glasgow, UK

(*Received* 24 *September* 2021; *revised* 29 *April* 2022; *in final form* 2 *May* 2022)

Abstract—Ultrasound accelerates healing in fractured bone; however, the mechanisms responsible are poorly understood. Experimental setups and ultrasound exposures vary or are not adequately characterized across studies, resulting in inter-study variation and difficulty in concluding biological effects. This study investigated experimental variability introduced through the cell culture platform used. Continuous wave ultrasound (45 kHz; 10, 25 or 75 mW/cm^2, 5 min/d) was applied, using a Duoson device, to Saos-2 cells seeded in multiwell plates or Petri dishes. Pressure field and vibration quantification and finite-element modelling suggested formation of complex interference patterns, resulting in localized displacement and velocity gradients, more pronounced in multiwell plates. Cell experiments revealed lower metabolic activities in both culture platforms at higher ultrasound intensities and absence of mineralization in certain regions of multiwell plates but not in Petri dishes. Thus, the same transducer produced variable results in different cell culture platforms. Analysis on Petri dishes further revealed that higher intensities reduced vinculin expression and distorted cell morphology, while causing mitochondrial and endoplasmic reticulum damage and accumulation of cells in sub-G1 phase, leading to cell death. More defined experimental setups and reproducible ultrasound exposure systems are required to study the real effect of ultrasound on cells for development of effective ultrasound-based therapies not just limited to bone repair and regeneration. (E-mail: d.gupta@bham.ac.uk) © **2022 The Author(s). Published by Elsevier Inc. on behalf of World Federation for Ultrasound in Medicine & Biology. This is an open access article under the CC BY license (http://creativecommons.org/licenses/by/4.0/).**

Key Words: **Ultrasound, Saos-2 cells, Osteogenic differentiation, Bone, Standing waves, Experimental reproducibility.**

INTRODUCTION

Low-intensity ultrasound has been in clinical use for the treatment of non-union fractures since 1995, when clinical trials revealed it could accelerate healing by more than 30% (Heckman et al. 1994). Osteogenic differentiation, essential to the healing process, has been a focus of several studies that sought to understand the mechanism underlying this effect. A wide variety of osteogenic cells have been investigated, including primary cells, such as bone marrow–derived (Angle et al. 2011; Sant'Anna et al. 2005; Sena et al. 2011; Gao et al. 2016) or adipose-derived mesenchymal stem cells (Yue et al. 2013); osteoblasts derived from calvaria (Sun et al. 2001), femora, tibia, fibula, clavicle (Hasegawa et al. 2009) and of alveolar (Lim et al. 2013) and mandibular origin (Imai et al. 2014; Huang et al. 2015); osteocytes from femora (Naruse et al. 2003); periodontal ligament cells (Reher et al. 1997); gingival fibroblasts (Reher et al. 1998); and dental pulp stem cells (Gao et al. 2016) sourced from humans, rats and mice; and also some cell lines including human adipose stem cells (Uddin and Qin 2013), MC3T3-E1 cells (Man et al. 2012a), Saos-2 (McCormick et al. 2006) and

Address correspondence to: Dhanak Gupta, School of Dentistry, Institute of Clinical Sciences, College of Medical and Dental Sciences, University of Birmingham, 5 Mill Pool Way, Edgbaston, Birmingham B5 7EG, UK. E-mail: d.gupta@bham.ac.uk

ST2 and MDPC-23 cells (Scheven et al. 2007, 2009). Such studies also describe a wide variety of ultrasound exposure conditions with ultrasound frequencies ranging from 1−3 MHz down to 45 kHz (Azuma et al. 2006) operated in continuous and pulsed modes across a range of intensities (2−2000 mW/cm^2 spatial-average, temporal-average intensities [I_{SATA}]), duty cycles (20−50%, continuous) and exposure times (5−20 min).

While a number of methodologies have been used to expose cells *in vitro* to ultrasound, the majority of these studies utilize Exogen systems or ultrasound conditions that replicate them. Exogen (Bioventus LLC) is a commercial ultrasound bone healing system comprising an unfocused, circular aperture (diameter = 22 mm) ultrasound transducer with an operational frequency of 1.5 MHz, I_{SATA} of 30 mW/cm^2, pulse width of 200 μs, pulse repetition frequency of 1 kHz and duty cycle of 20%. Exogen is approved by the National Institute of Clinical Excellence (NICE) in the United Kingdom to treat patients with non-union fractures (NICE 2019) and by the Food and Drug Administration (FDA) in the United States (Aliabouzar et al. 2018). Several studies have coupled one or more of these transducers to the base of multiwell plates (typically) or Petri dishes, using acoustic couplant to promote sound transmission, as a basis to investigate the effect of pulsed ultrasound on cellular activities. Studies using Exogen systems claim that ultrasound upregulates COX2, PGE2, BMP2, BMP4, BMP6 and BMP7, increases cell division in periosteal cells, upregulates growth factors that trigger new blood cells, increases bone mineral density, upregulates endochondral ossification and enhances osteoblast differentiation (Padilla et al. 2014).

The Duoson ultrasound device (SRA Developments, Devon, UK) offers a clinical alternative to the Exogen and can be operated at two frequencies, 45 kHz and 1 MHz. In studies where this device was employed, it was commonly positioned above a well plate or Petri dish, with the transducer dipped into the culture medium to couple the propagating sound to the plated cells (Fig. 1). Other devices investigated include ultrasonic tips, inspired by traditional dentistry tools, that can be employed *in vitro* by inserting them within cell culture dishes (Sura et al. 2001; Scheven et al. 2009). However, all of these systems have limitations, including damping arising from the tissue culture plastic (polystyrene) itself; interference patterns developed because of polystyrene or glass at the base or walls of the wells that influence the acoustic field experienced (potential for cells to be subjected to large, localized gradients of displacement, velocity and acoustic pressure); and overheating leading to thermal effects (Padilla et al. 2014). In addition, when the ultrasound is applied, surface waves will be produced on the liquid, which may lead to disturbance of the medium. There will be complex longitudinal waves produced inside the dishes, which may lead to varying amounts of potential resonance. Cells will receive different sound levels depending on whether any resonance takes place during exposure.

This, in conjunction with the range of cell culture platforms used and the wide variety of acoustic parameters, has led to significant inter-study variation in the literature. Such inter-study variation makes the direct comparison between studies difficult and, therefore, precludes formulation of meaningful conclusions regarding reproducible and real biological effects occurring because of ultrasound *in vitro*. We propose that standardization of experimental setups and a better understanding of the acoustic doses delivered to the cells under investigation are required.

This study investigated how the selection of the cell culture platform used, in conjunction with the Duoson device, which has an anterior face diameter of 30 mm, influences the effects of ultrasound treatment on Saos-2 osteoblast-like cells. Two different culture vessels were investigated, multiwell (6-well) plates and single well (Petri dish), each with a well diameter of 35 mm. We aimed to determine the suitability of these vessels for

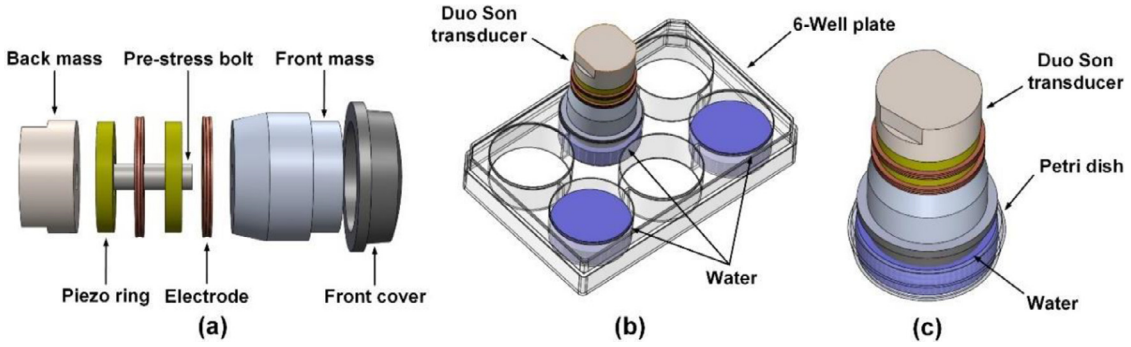

Fig. 1. Configuration of Duoson transducer. (a) Exploded view of the Duoson transducer. (b) Transducer in the 6-well plate. (c) Transducer in the 35-mm Petri dish.

investigating the effects of ultrasound on cells *in vitro* and this work may be applicable to other *in vitro* studies that investigate the effect of ultrasound on cells.

METHODS

Ultrasonic characterization of the Duoson transducer

The Duoson is a dual-frequency therapeutic ultrasound device with eight modes of operation at 1 MHz, 45 kHz or both. Throughout this study, the 45-kHz frequency was employed, namely, Modes I, II and III, which operate in continuous wave. This frequency has been suggested to be therapeutic in previous studies (Reher et al. 1998; Maddi et al. 2006; Man et al. 2012b). The associated power and I_{SATA} values (as determined by the manufacturer with radiation force balance measurement) are listed in Table 1.

Vibration response of the transducer. The Duoson utilises a standard bolted Langevin-style transducer consisting of front and back metal masses sandwiching a stack of piezoceramic elements by means of a pre-stress bolt (Fig. 1a). The piezoceramic stack is excited with an alternating current signal at a specified frequency, leading to excitation of ultrasonic vibration of the same frequency that propagates through the metal waveguide to the anterior (front) face of the transducer. The Duoson device was used to expose cells, plated in two different culture platforms, to ultrasound (Fig. 1b, 1c). In the multiwell (6-well) plate, the Duoson transducer anterior face was immersed in the water in the middle-top well, and the two wells positioned diagonally to this were also filled with water (to mimic the cell culture experiments as the cells were seeded in these alternating wells). In the Petri dish, the transducer was directly immersed in the water. In all cases, the diameter of the wells was 35 mm.

A 1-D laser Doppler vibrometer (OFV 303, Polytec GmbH, Waldbronn, Baden-Württemberg, Germany) was used to measure the normal-to-surface vibration displacement response on the anterior face of the Duoson transducer in air in the pre-set modes of operation I, II and III (Fig. 2a). Measurements were acquired from a grid of measurement points on the curved anterior transducer face in radial increments of 5 mm (Fig. 2b), with reflective tape used to increase the reflected signal at each grid point. It should be noted that the central metal nib was not part of the 45-kHz transducer mode.

Table 1. Duoson 45-kHz operational modes with custom-designed associated power and spatial-average, temporal-average intensity (I_{SATA})

Mode	Power (mW)	Intensity (mW/cm^2)
I	160	10
II	406	25
III	1217	75

Finite-element models of the transducer inserted in cell culture dishes. Models of the Duoson transducer, both in a free condition and inserted in a 6-well plate or Petri dish, were created using finite-element analysis (FEA) software (OnScale, Redwood City, CA, USA). The FEA models of the transducer immersed in a 6-well plate or Petri dish were developed initially in CAD software (SolidWorks, Dassault Systemes, Paris, France), as illustrated in Figure 1, and then imported into the FEA software OnScale. Material properties were assigned to each component of the assembly. The transducer, well plate and water boundaries were defined by a change in impedance, and the boundary condition of the external faces of the whole model was defined by contact with water, to mimic the experimental setup in which the whole well plate was partially immersed in water to half-height of the well plate. The mesh incorporated 40 elements per wavelength.

The models were all developed to match the conditions of the experiments. In each model that incorporated a well plate, the wells were filled with 6.5 mL of water (Fig. 1b, 1c). For the 6-well plate, the depth of each well was 15.7 mm, and the water depth in the well was 8 mm. For the 35-mm Petri dish, the depth of the well was 9.35 mm, and the depth of water was 8 mm. For all models, the anterior face of the transducer was set at a height of 5 mm from the base of the well. For Mode I (10 mW/cm^2), Mode II (25 mW/cm^2) and Mode III (75 mW/cm^2), a continuous ultrasound wave was applied. The FEA models were then used to calculate characteristics of the transducer in air and in the two different well-plate configurations (6-well plate and single Petri dish). The change in resonance frequency of the transducer in water was calculated to investigate the effect of water loading. The vibration displacement amplitude in resonance in air of the transducer's anterior face was calculated for the three acoustic intensities of Modes I, II and III, to allow for verification of the FEA model from vibration displacement measurement data using a laser vibrometer. Calculation of the electrical impedance of the transducer revealed the change from air to water loading, providing an indication of the significance of loading between the two well-plate configurations. Finally, the acoustic pressure field in the water-filled wells and the vibration displacement field of the culture platforms were calculated.

Acoustic pressure field measurement. The acoustic pressure field produced by the Duoson transducer was measured in a scanning tank (600 × 900 × 600 mm) filled to a depth of 400 mm with de-gassed, de-ionized

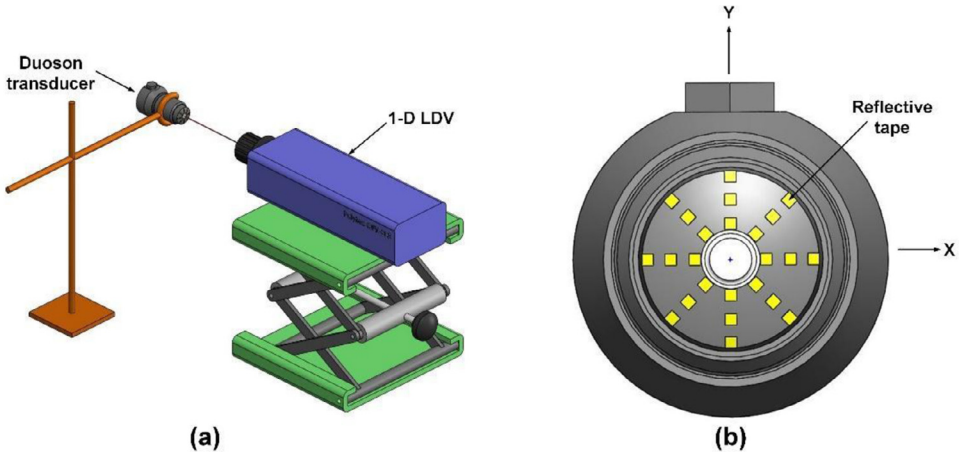

Fig. 2. Setup for vibration measurement of the Duoson device. (a) Schematic of the laser Doppler vibrometer (LDV) measurement. (b) Measurement grid (using reflective tape) on the anterior face of the transducer.

water heated to 37 ± 2°C. Pressure measurements were made using a 2-mm−diameter needle hydrophone (Precision Acoustics, Dorchester, UK) aligned to the center of the Duoson anterior face and mounted on a precision XYZ motorized stage (Fig. 3a) with linear resolution 62.5 μm.

Root mean square (RMS) and peak negative pressures ($p-$) were acquired in the XY plane at propagation distances (Z) of 3 and 5 mm from the anterior face of the transducer to a distance ±20 mm of the beam center and increments of 1 mm.

Acoustic pressure field measurements were hindered by the formation of bubbles around the central nib of the transducer anterior face (Fig. 3b). Inspection of the device patent (Young and Bradnock 2003) revealed that the central nib material was aluminium. It is suspected that the bubbles were caused primarily by oxidation of the aluminum, possibly because of a galvanic reaction with other more noble metals submerged in the tank (steel rod or stainless steel/bronze of the needle hydrophone housing). The presence of these bubbles induced cavitation in the higher-intensity modes, so pressure measurements were limited to Mode I only.

To minimize the errors associated with the bubble formation, a maximum amplitude approach was employed and measurements were averaged. An acoustic absorber (SF5048, Precision Acoustics, Dorchester, UK) was used to minimize ultrasound wave reflections within the tank. The hydrophone output was routed via its preamplifier and DC coupler to an oscilloscope (DPO7054, Tektronix, Beaverton, OR, USA) and received at a PC via a GPIB interface. All voltage waveforms were stored as position-stamped delimited text files for further analysis.

Voltage waveforms were converted to pressure (1.639 μV/Pa at 45 kHz). Finally, assuming radial symmetry, peak negative pressures were extrapolated to produce acoustic field maps in the XY plane to illustrate the free-field beam shape.

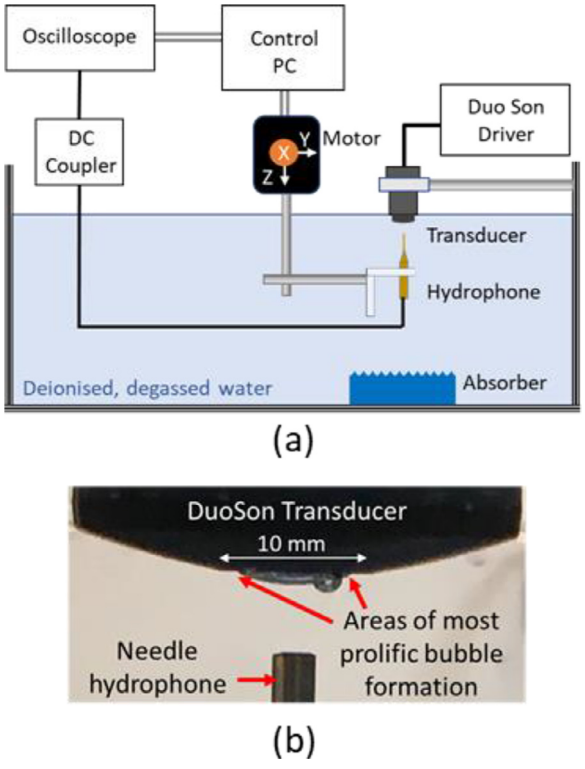

Fig. 3. (a) Setup for acoustic field measurement of the Duoson transducer. (b) Positions of transducer and hydrophone and image of bubble formation.

Cell-based experiments

All materials were purchased from Thermo Fisher Scientific (Gloucester, UK) unless otherwise specified.

Saos-2 cell culture. Saos-2 cells derived from osteosarcoma tissue were cultured in standard culture medium, that is, McCoy's 5A medium supplemented with 10% (v/v) foetal bovine serum, 100 U/mL penicillin, 100 μg/mL streptomycin and 1 mM L-glutamine at 37˚C in a humidified atmosphere with 5% CO_2 to 70%−90% confluency.

For metabolic activity per well assessment over short periods of culture (4 d), cells were seeded at 10,000 cells/cm^2, and the next day (day 1), after changing the culture medium, ultrasound treatment was started. Ultrasound was further applied on days 2 and 3. On day 4, metabolic activity per well was assessed as described below. Cells were exposed to ultrasound for a duration of 5 min/d at a frequency of 45 kHz, with the power and intensities (SATA) defined in Table 1. In all cases, the transducer was positioned at a distance of 5 mm from the cell surface, with the transducer anterior face submerged in the culture medium for ease of acoustic coupling.

For osteogenic differentiation, cells were seeded at 10,000 cells/cm^2, and on day 2 culture medium was replaced with osteogenic culture medium, that is, standard culture medium supplemented with 50 μg/mL ascorbic acid 2-phosphate and 0.5 mM β-glycerophosphate. Then cells were treated with ultrasound as described above, and this treatment was continued for a further 9 d. Ten days after the addition of the osteogenic supplements, calcium deposition was assessed using an Alizarin Red S assay as described below.

To assess the effect of ultrasound treatment on cell attachment in Petri dishes, cells were seeded at 10,000 cells/cm^2 and ultrasound was applied immediately. Post-treatment, cells were aliquoted in volumes of 250 μL and transferred to 48-well plates for metabolic activity assessment and also in volumes of 100 μL to eight-well μ-slides (Ibidi, Thistle Scientific LTD, Glasgow, UK) for assessment of actin and vinculin the next day as described below.

Ultrasound exposure setup. Cells plated in either 6-well plates or Petri dishes were each treated with ultrasound using Modes I, II and III. The 6-well plate (Fig. 1b) was positioned in a custom-built anti-reflective chamber containing water maintained at 37˚C. Cells were seeded in three wells at a time as illustrated in Figure 1b. This step was taken because a previous study indicated significant lateral propagation of ultrasound to adjacent wells (Patel et al. 2015). The distance between the base of the well plate where the cells attached and the transducer anterior face was 5 mm. To treat cells within Petri dishes (Fig. 1c), the transducer was mounted in a fixed vertical position, and each Petri dish was sequentially mounted into a concentrically aligned jig and raised on a precision vertical stage (LJ750/M, Thorlabs, Ely, UK) to a pre-set insertion depth corresponding to a 5-mm separation between the bottom of the culture dish and the transducer tip. In both configurations, a control condition was used in which the transducer was submerged into the same culture platform but no ultrasound energy was applied (0 mW/cm^2).

PrestoBlue® assay. PrestoBlue® is a resazurin-based dye that is reduced in the mitochondria of living cells and converted into a red fluorescent resorufin that can be detected and extrapolated to quantify metabolic activity. Prestoblue® assay was used to assess the metabolic activity per well of Saos2 cells after ultrasound treatment. On each time point, culture medium was removed, and cells were washed with phosphate-buffered saline (PBS) before adding the PrestoBlue® working solution prepared by mixing the PrestoBlue® reagent with pre-warmed Hanks' balanced salt solution at a ratio of 1:9 (v/v). Three wells containing only the working solution with no cells were used as blanks. During the kinetic phase of reactions, 100-μL aliquots per well were taken after gentle mixing of cells, and the fluorescence intensity was measured using 530-nm−excitation and 590-nm−emission filters on a microplate reader (Tecan, Thale, UK).

The mean metabolic activity per well was expressed as mean fluorescence intensity measured after subtracting the reading for unreduced (blank) reagent and normalising to the reaction time.

Alizarin Red S assay. Calcium deposited by the cells in the extracellular matrix was assessed using the Alizarin Red S assay. Culture medium was removed, and cells were washed once with PBS at room temperature for 5 min, before fixation using 3.7% paraformaldehyde in PBS for 10 min. After the fixative was removed, cells were again washed with PBS and then stained with a 1% (w/v) solution of Alizarin Red S (pH 4.2) for 30 min at room temperature. Once the staining solution was removed and cells were washed with de-ionized water to remove any unbound stain, cells were imaged using a Nikon Eclipse TE300 microscope (Nikon Europe BV, Amsterdam, Netherlands) connected to a Nikon D5100 camera (Nikon Europe BV).

Actin and vinculin staining. To assess cell attachment, actin and vinculin staining was performed. The culture medium was removed, and cells were washed once with Dulbecco's phosphate-buffered saline (DPBS) before fixation with 3.7% paraformaldehyde in PBS for 10 min at room temperature. Samples were permeabilized with 0.1% Triton X-100 in DPBS for 1 h and stained with 10 μg/mL Alexa Fluor 488 anti-vinculin

antibody (53-9777-82, Thermo Fisher Scientific) overnight at 4˚C. On the next day, after being washed with DPBS, cells were stained with 100 nM Acti-stain 555 phalloidin (PHDH1, Cytoskeleton, Inc., Denver, CO, USA) and 1 μg/mL 4′,6-diamidino-2-phenylindole (DAPI) in DPBS for 30 min at room temperature. Finally, cells were washed with DPBS and visualized using a Zeiss LSM780 confocal microscope (Carl Zeiss MicroImaging GmbH, Jena, Germany) with a 40 × lens.

Propidium iodide staining. Propidium iodide (PI) is a fluorescent nucleic acid dye that can be used to quantify the proportion of cells in one of the three interphase stages of the cell cycle. PI staining was undertaken after cells were treated with ultrasound. Cells were seeded at 10,000 cells/cm^2 in Petri dishes and left overnight to attach. On the following day, culture medium was changed, cells were treated with ultrasound and immediately the culture medium was transferred to a new tube; the remaining cells were detached using 0.25% (w/v) trypsin and 1 mM EDTA and transferred to the same tube as the culture medium. The cell suspensions were pelleted, washed using DPBS, then fixed using 1 mL of 70% ethanol before again washing twice with DPBS. Finally, for PI staining, 300 μL of PI working solution (50 μg/mL PI in DPBS) and 50 μL of RNase working solution (0.3 μL/mL of RNase A in DPBS) was added and samples were incubated at 37˚C for 1 h before being left undisturbed overnight at 4˚C. On the next day, samples were analysed using FACSCalibur (BD Biosciences, Ashland, OR, USA) and Flow Jo 10.6.0 software (BD Biosciences).

Transmission electron microscopy

Cells were seeded at 10,000 cells/cm^2 in Petri dishes, and ultrasound (mode III) was applied immediately for 5 min. Post-treatment, cells were collected and pelleted, and samples were washed with DPBS and fixed using 2.5% glutaraldehyde in 0.1 M PBS. Subsequently, samples were treated with 1% osmium tetroxide in 0.1 M PBS, dehydrated in graded ethanol solutions 2 × 50%, 2 × 70%, 2 × 90%, 2 × 100% and 2 × 100% ethanol for 15 min each step. Samples were treated with propylene oxide twice, refreshed after 15 min, followed by propylene oxide/resin solution (1:1) overnight on a rotator before being embedded in fresh Epon epoxy resin, prior to polymerization, for at least 16 h at 60˚C. Samples approximately 90 nm thick were sectioned using an ultramicrotome (Ultracut E, Reichert Jung Limited, Cambridge, UK), placed on 200-mesh copper Formvar-coated grids and stained with 30% uranyl acetate for 7 min. Sections were washed three times with sonicated ultrapure water, dried using a filter paper and further stained with Reynolds lead citrate for 7 min before being washed with sonicated ultrapure water. Finally, sections were examined using a transmission electron microscope (JEM-1400 120kV, Hertz, JEOL (UK) Ltd.) using an accelerating voltage of 80 kV. Electron micrographs were recorded using a Morada 3.0 soft imaging system (EMSIS GmbH, Münster, Germany).

Statistical analysis

All statistical analyses were performed using GraphPad Prism 8, version 8.2.0. (San Diego, CA, USA). The mean and standard error of mean (SEM) were computed for at least three replicate samples in all experiments and one-way or two-way analysis of variance was performed. Ultrasound intensity and day of culture were two fixed factors. For pairwise comparisons, *post hoc* analyses using least significant difference, equivalent to no adjustments, were carried out. P values <0.05 were considered to indicate significant difference.

RESULTS

Ultrasonic characterization

Vibration response and acoustic pressure measurements were used to validate the FEA of the Duoson transducer such that the vibration and pressure amplitude distributions generated within both 6-well plates and Petri dishes during *in vitro* ultrasound exposures could be estimated and correlated with data collected from the cell culture experiments.

Vibration response of the 45-kHz transducer in experiments. From the laser vibrometer measurements, when the transducer is vibrating in air under free conditions (Fig. 4), the displacement is dependent on the drive power applied to the transducer and, therefore, increases from Mode I to Mode II to Mode III. X and Y are horizontal and vertical coordinates of the transducer anterior face, with the origin (0,0) located at the transducer's central axis. The axial displacement amplitudes are illustrated for all the measurements points in Figure 4.

There is a 127% increase in displacement amplitude at the inner circumference of the anterior face from Mode I to Mode III. Vibration displacement amplitude is highest at the inner circumference and lowest at the outer circumference. The displacement fields in Figure 4 are not precisely radially symmetric, despite the transducer face being symmetrical. This meant that the acoustic field sensed by cells in the well plates may not be exactly as predicted by the FEA model, which assumes radial symmetry, but the difference may be small.

Transducer FEA model. From the FEA of the transducer, the resonance frequency of the 1st longitudinal mode is calculated from the electrical impedance as

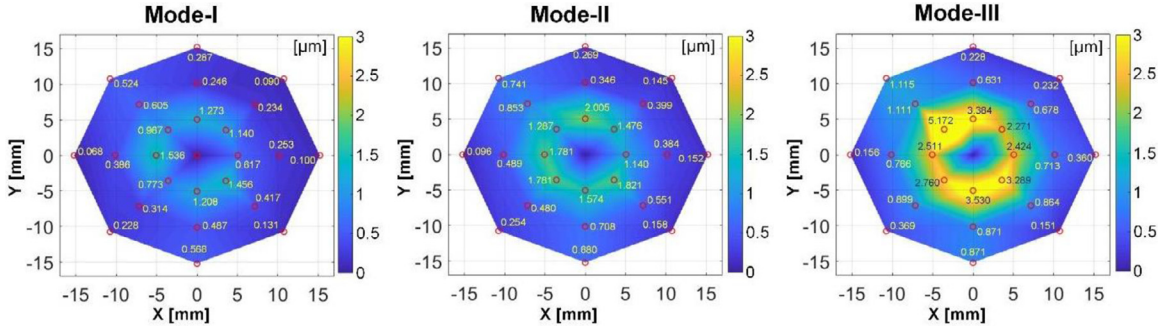

Fig. 4. Vibration displacement amplitude measured at the anterior face of the transducer for Modes I, II and III.

44.63 kHz (Fig. 5a), compared with 45.8 kHz from the laser vibrometer measurements. Figure 5b and 5c illustrate that the resonance frequency increases by around 4 kHz when the water and well contact loads are introduced by immersing the transducer into the 6-well plate or Petri dish.

To match the experimental measurements of the vibration displacement amplitude, the voltages applied to the piezoceramic stack in the FEA models were set at 2.2, 3.1 and 5.5 V for Modes I, II and III intensities, respectively. When immersed in water, as with the transducer placed in the 6-well plate or the Petri dish, the resonance frequencies increased by approximately 4 kHz, and the impedance increased to 496.4 and 227.6 Ω, respectively, results that are consistent with a previous study using the Duoson device (Patel et al. 2015). Through use of the same applied voltages to the piezoceramic elements, the vibration displacement amplitude at the anterior face of the transducer decreased when placed into water, and attenuation was greater in the 6-well plate than in the Petri dish as a result of the higher impedance. These FEA results suggest that the transducer would excite lower vibration levels when configured with a 6-well plate than with a Petri dish.

Simulation of the transducer immersed into cell culture platforms. FEA predictions of the vibration displacement distribution on the surfaces of the culture platforms (well plate and Petri dish) when ultrasound was applied using the Duoson device are illustrated in Figure 6. The results indicate that standing wave patterns are excited in both cell culture configurations. The ultrasound propagates through the walls of the 6-well plate into other wells (Fig. 6a) even when adjacent wells are not filled with water. The vibration displacement of the anterior face of the transducer exhibits some asymmetry (Fig. 6b), even though the applied displacement of the transducer is radially symmetric in the FEA model, because the load is asymmetric. In the case of the 35-mm Petri dish, the load is symmetric and, therefore, the displacement of the transducer is symmetric, which was transmitted to the Petri dish as well (Fig. 6e–h).

The pressure field on the top and bottom surfaces of the water volumes in the three water-filled wells of the 6-well plate are illustrated in Figure 6 (c, d). For the two water volumes with a free top surface, there was an acoustic field excited throughout the water volume, which diminishes to zero on the free surfaces, where the acoustic field is excited by direct (via contact with the well plate) and indirect (through the directly excited water volume) vibration transmission from the transducer.

A 50-ms time domain simulation in FEA was performed for the three acoustic intensities, first to estimate

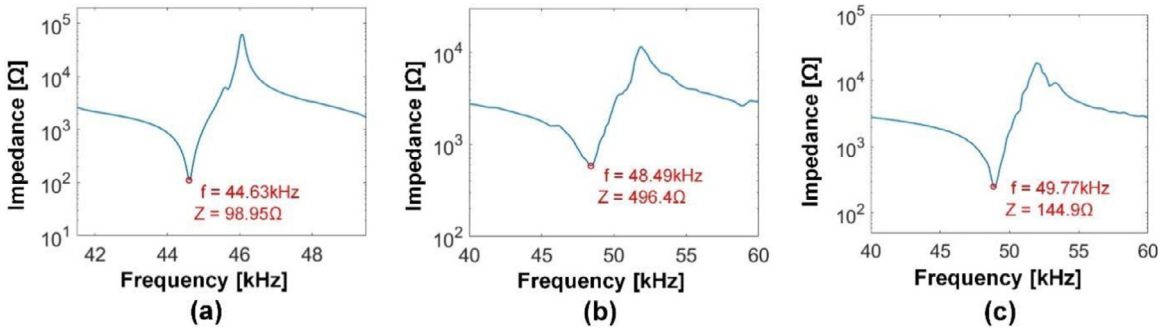

Fig. 5. Finite-element analysis–predicted free response of the transducer. (a) Impedance in free air. (b, c) Impedance of the transducer immersed in a (b) 6-well plate and (c) 35-mm Petri dish.

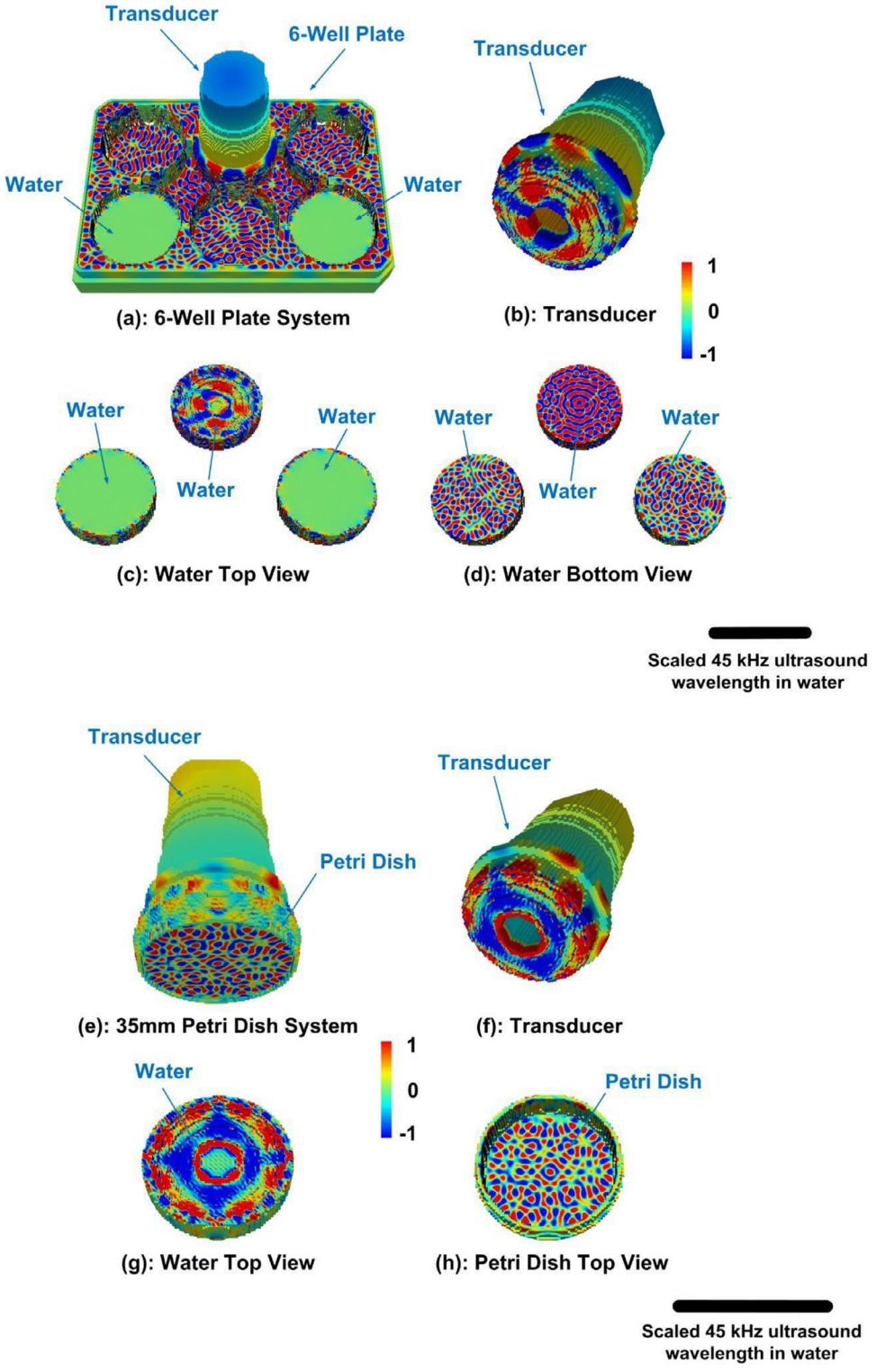

Fig. 6. Finite-element analysis–predicted normalized displacement of the transducer and normalized pressure field in water for the transducer immersed into a (a–d) 6-well plate and (e–h) 35-mm Petri dish. *Red* and *blue* indicate the regions of maximal displacement (with *red* and *blue* being out-of-phase with each other) and *yellow*/*green* indicates nodal lines/regions.

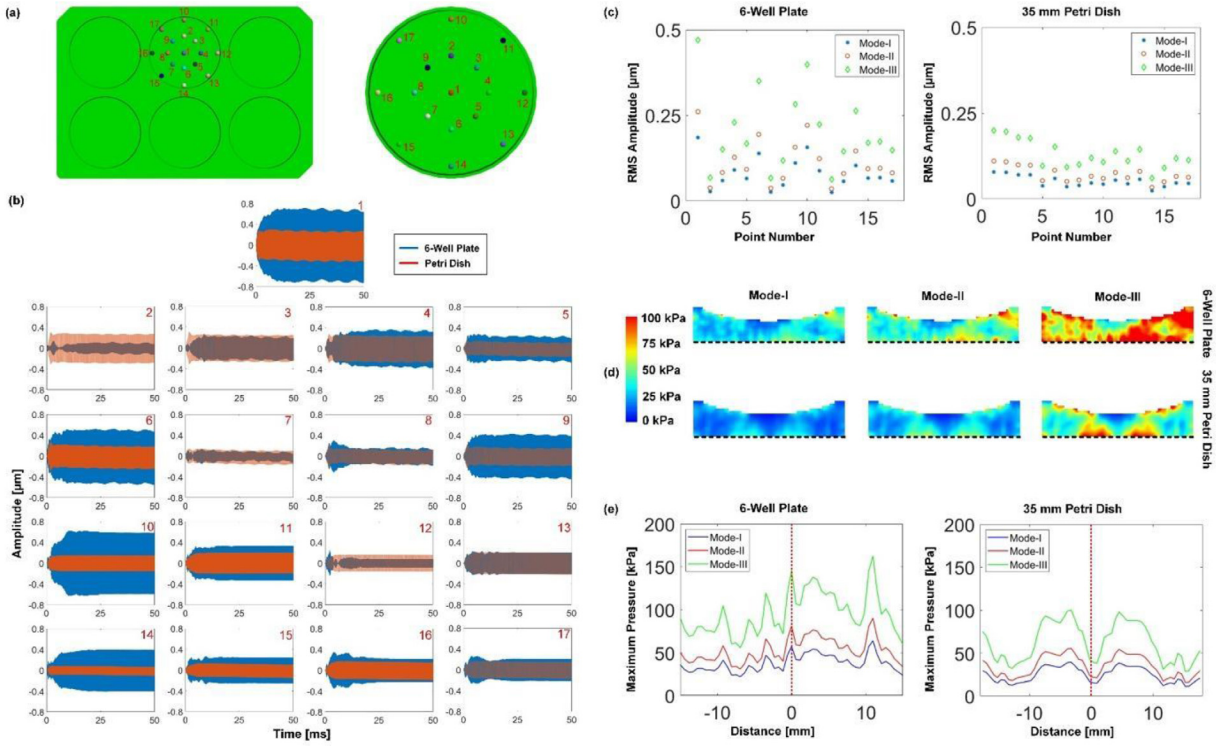

Fig. 7. Response of the cell culture systems to the ultrasound transducer. (a) Location of 17 points at the bottom of one of the wells (35 mm wide) of a 6-well plate and 35-mm−wide Petri dish. (b) Vibration amplitude of the 17 points at Mode III. (c) Root mean square amplitude of 17 points for the 6-well plate and 35-mm Petri dish. (d) Acoustic pressure field in a cross-section of water for the 6-well plate and 35-mm Petri dish. (e) Pressure along the *black dashed lines* in (d). The *red dotted line* marks the center of the well/dish.

Table 2. Finite-element analysis–predicted root mean square values of displacement of the polystyrene base, and pressure at the base of the associated water volumes, of the 6-well plate and Petri dish from 17 locations*

Platform	Vibration displacement amplitude (μm)			Acoustic pressure (kPa)		
	Mode I	Mode II	Mode III	Mode I	Mode II	Mode III
6-well plate	0.08 ± 0.05†	0.11 ± 0.06	0.20 ± 0.12	37.8 ± 9.8	53.3 ± 13.9	96.1 ± 25.0
35-mm Petri dish	0.05 ± 0.02	0.07 ± 0.02	0.13 ± 0.04	24.6 ± 8.9	34.7 ± 12.6	62.7 ± 22.7

* See Figure 7.
† Mean ± standard deviation.

the displacement amplitude of the polystyrene base of the 6-well plate and 35-mm Petri dish and subsequently to estimate the acoustic pressure field in the water in the two cell culture platforms, where cells would be located in ultrasound experiments. The results are illustrated in Figure 7a–e and Table 2.

The base of the 6-well plate vibrated with at least 35% higher mean displacement amplitude in steady state than the 35-mm Petri dish, but the standard deviations for the displacement across the 17 points in the 6-well plate is much higher for modes I, II and III (Fig. 7b, 7c).

The predicted acoustic pressure in the water at the central cross-section (at the diameter from point 10 to point 14 in Fig. 7a) is shown for Modes I, II and III in Figure 7d, with the peak pressure increasing with intensity, agreeing with the displacement and pressure field distributions shown in Figure 6. The Figure 7e plots the predicted acoustic pressure along a diameter (*black dashed line* in Fig. 7d) at the base of the water volume, with the mean of the acoustic pressure also recorded in Table 2. The Figure 7e illustrates the symmetry of the pressure field in the Petri dish compared with the 6-well plate at the location where cells are seeded in typical ultrasound experiments.

Measured acoustic pressure field excited by the transducer. The measured average RMS pressure (Fig. 8a) at 3 mm from the center of the anterior face of the transducer revealed a three-peak beam shape, with the highest pressures (16.6 kPa) occurring 10 mm from the beam center in both positive and negative directions and a smaller central peak of 14.1 kPa. The standard

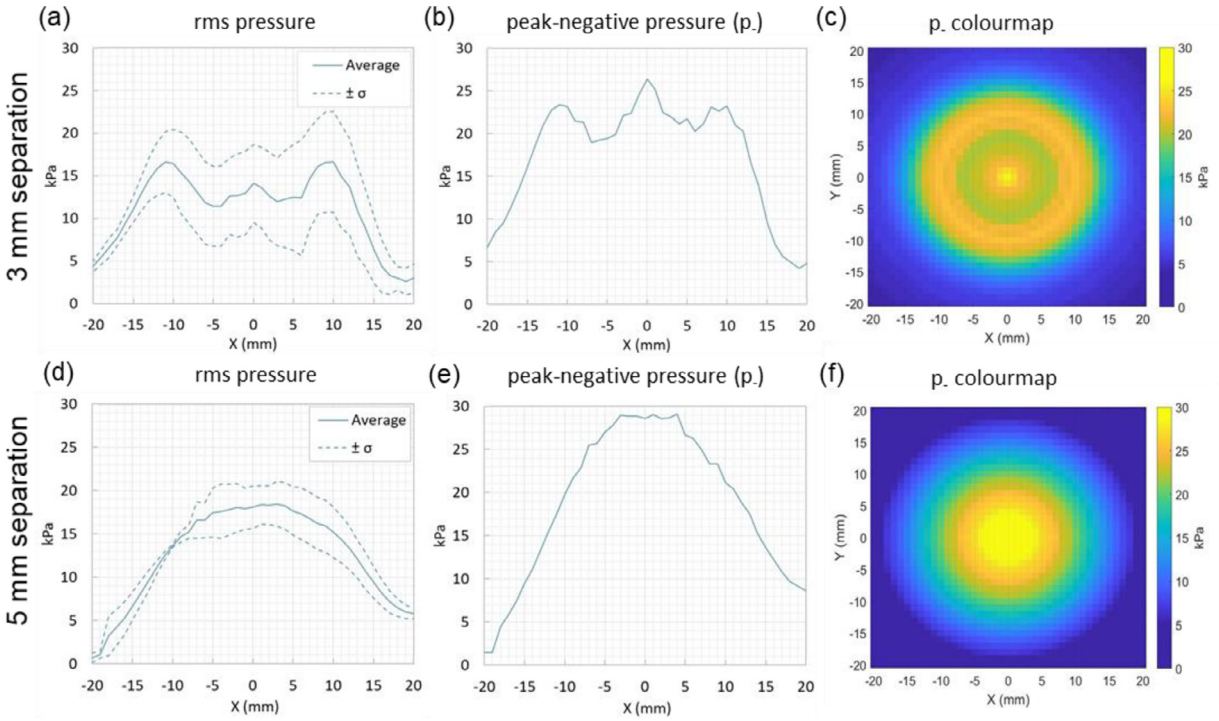

Fig. 8. Pressure field of the Duoson transducer in Mode I at 3- and 5-mm separations from the center of the transducer anterior face in free field conditions. (a, d) Root mean square pressure with standard deviation σ (N = 5 at 3 mm, N = 2 at 5 mm). (b, e) Average peak negative pressure (p_-). (c, f) Color maps of peak negative pressure extrapolated from (b) and (e) averaged either side of the beam center to indicate the cross-sectional pressure distribution.

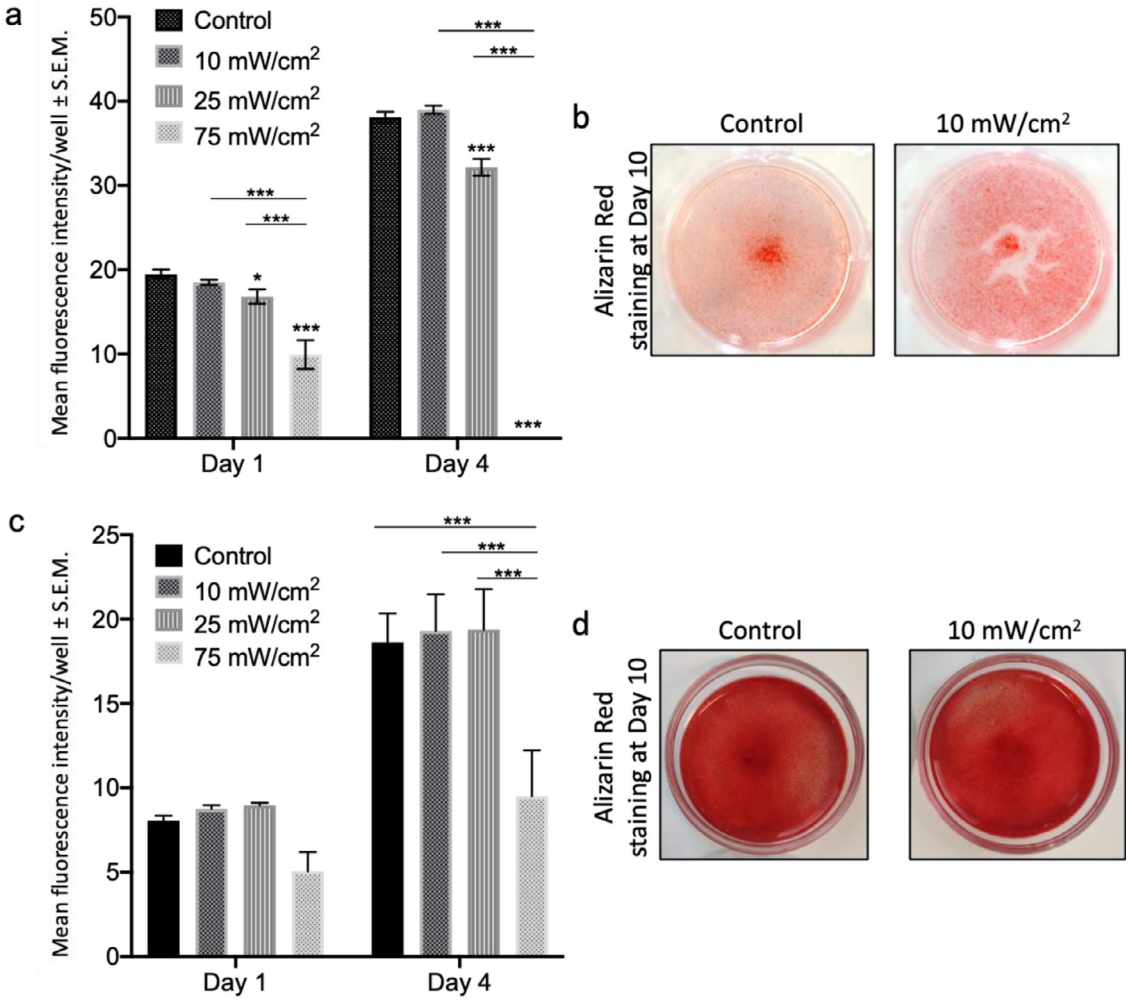

Fig. 9. Effect of different ultrasound intensities on Saos-2 cells in 6-well plates (a, b) and 35-mm Petri dishes (c, d). (a, c) Mean ± S.E.M. of metabolic activity per well over 4 d ($n \geq 15$). *$p < 0.05$, ***$p < 0.001$ compared with controls unless indicated. (b, d) Alizarin Red staining after 10 d in osteogenic medium. In the case of 6-well plates only, there was a clear area around the center of the well that was devoid of cells and calcium deposition in the 10 mW/cm^2 condition that was not observed in controls.

deviation was high (average 37%) because of bubble formation and the issues with continuous wave measurements mentioned under Methods. The peak negative pressure (Fig. 8b) revealed the same three peaks but with the highest amplitude of 26.4 kPa in the center. The beam shape extrapolated from this distribution (Fig. 8c) showed the central peak with a ring of high pressure (23.4 kPa) in a 10-mm radius around the center. The RMS pressure data at 5 mm from center of the anterior face of the transducer (Fig. 8d) revealed a beam shape with a single peak and smoother roll-off, with maximum pressures in the center of the beam ranging from 17.5 to 18.5 kPa. The standard deviation was, on average, 15% lower than found at 3 mm. The half-pressure beam width, which is the distance between the two points at which the pressure reaches one-half of the maximum, was 28 mm, compared with the 35-mm diameter of the culture platforms. The peak negative pressure (Fig. 8e) had a similar beam shape, with amplitudes up to 29 kPa. The extrapolated beam shape (Fig. 8f) had a single circular beam shape with a smoother amplitude distribution.

Cellular responses to ultrasound in 6-well plates

In 6-well plates, metabolic activity per well was assessed on days 1 and 4 of culture (Fig. 9a). There was a decrease in mean metabolic activity per well with increased ultrasound intensity from 10 to 75 mW/cm^2 ($p < 0.05$) at both time points. Mineralization was assessed after 10 days with or without exposure to 10 mW/cm^2 ultrasound intensity. In ultrasound-treated wells, there was a clear region in the center (Fig. 9b) that

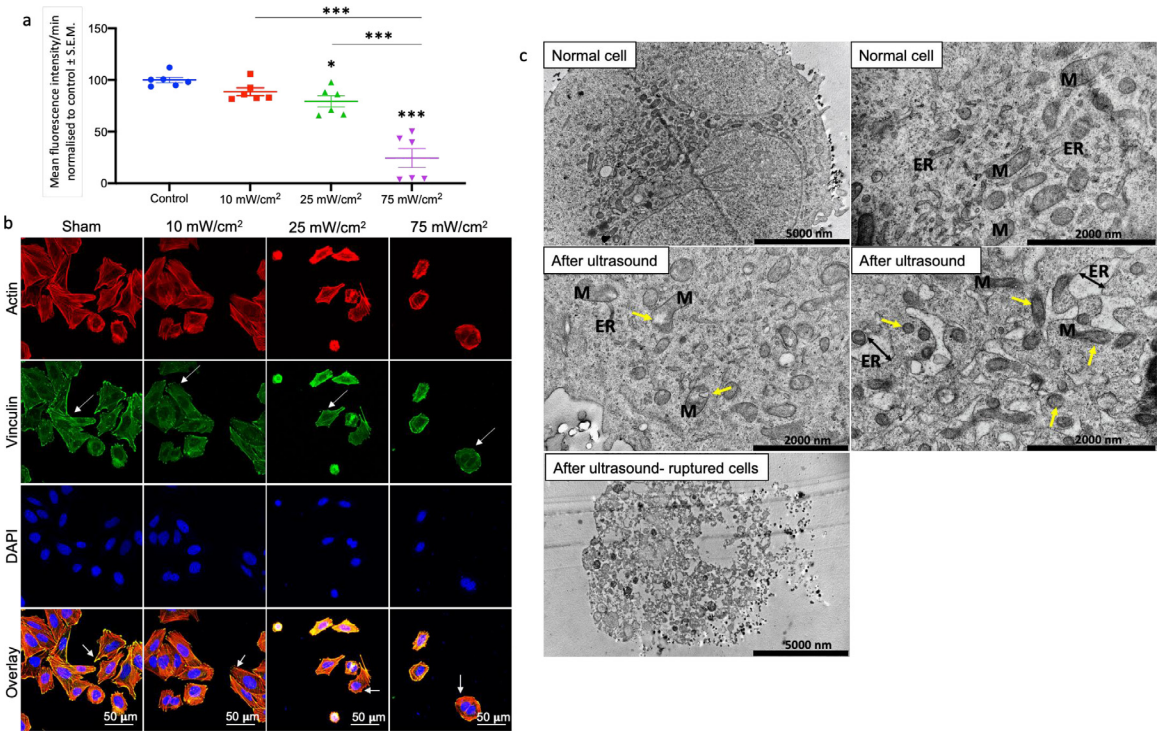

Fig. 10. Reduced Saos-2 cell attachment as an effect of ultrasound. (a) Mean ± S.E.M. of metabolic activity per well measured 24 h after treatment (n = 6). *$p < 0.05$, ***$p < 0.001$ compared with control unless indicated otherwise. (b) Representative vinculin, actin and DAPI stained cells with overlays 24 h after treatment. *Arrows* indicate vinculin stain. (c) Ultrasound caused ultrastructure damage in Saos-2 cells. TEM images of cells in control (normal cells) and at 75 mW/cm^2 ultrasound intensity are shown. Note the increased size of endoplasmic reticulum (ER, double-sided arrows) and increased density and presence of ruptures (*yellow arrows*) in some of the mitochondria (M) after ultrasound treatment that were not observed in normal cells.

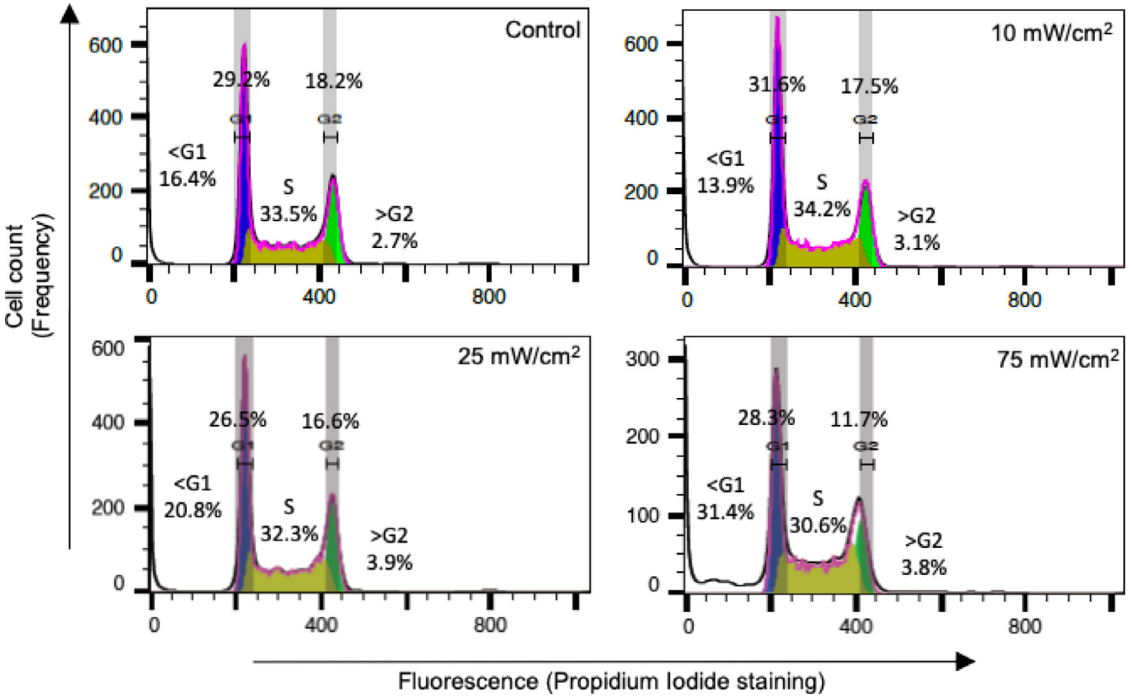

Fig. 11. Propidium iodide uptake analysis to assess impact of ultrasound treatment on cell cycle. *Blue, brown* and *green* regions depict cells in G1, S and G2 phases (n = 1). Note that the sub-G1 (<G1) cell population increased at higher ultrasound intensities compared with the control condition. This indicated an increase in both cell death and accumulation of cell debris as the ultrasound intensity increased.

was devoid of cells and calcium deposition, which was not present in controls.

Cellular responses to ultrasound in 35-mm Petri dish

Mean metabolic activity per well and matrix mineralization were also investigated for cells seeded in Petri dishes while exposed to ultrasound. There was significantly lower mean metabolic activity per well for the 75 mW/cm^2 condition compared with all other conditions on day 4 ($p < 0.001$, Fig. 9c). Alizarin Red staining after 10 days in osteogenic medium showed the formation of mineralized matrix across the entire Petri dish both for controls and under 10 mW/cm^2 conditions, unlike that observed in the 6-well plates (Fig. 9d).

As there was no crossover of ultrasound from one biological replicate to another in Petri dishes, further investigations were carried out using this setup. To assess the effect of ultrasound on cell attachment, cells were seeded on Petri dishes and immediately exposed to ultrasound for 5 min at different intensities. On the next day, the metabolic activity per well assessment was performed, which showed a reduction in metabolic activity of cells as ultrasound intensity increased (Fig. 10a). Cytoskeletal staining (Fig. 10b) revealed that the cells that were not exposed to ultrasound had an angular morphology with intense vinculin expression apparent in the cell periphery. In the 10 mW/cm^2 condition however, the intensity of vinculin staining was only slightly reduced, and for the 25 and 75 mW/cm^2 conditions, the cells exhibited a distorted morphology with accumulation of cortical actin and much reduced vinculin staining, as observed through visual inspection. TEM was also performed to examine the ultrastructure of cells after the ultrasound treatment. There was swelling (increased internal area of tubules in the TEM cross-section) of the endoplasmic reticulum and membrane damage in some mitochondria after treatment with ultrasound and evidence of ruptured cells only in the treated sample was also present (Fig. 10c). Finally, to assess the effect of ultrasound on cell cycle, PI staining was performed. The G2 population dropped from 18.2% to 11.7%, and the sub-G1 population increased from 16.4% to 31.4% in comparison with controls following 75 mW/cm^2 exposure (Fig. 11). This confirmed significant cell death and formation of cell debris after application of higher doses of ultrasound intensity.

DISCUSSION

A commercially available Duoson ultrasound therapy unit, which has been previously used for application of ultrasound *in vitro* (Man et al. 2012a; Ghorayeb et al. 2013; Patel et al. 2015; Gao et al. 2016, 2017), was used in this study in continuous wave mode at a resonant frequency of 45 kHz and at three set

intensities of 10, 25 and 75 mW/cm^2. Ultrasound was applied to Saos-2 cells seeded on tissue culture plastic in two different culture platforms, namely, 6-well plates and Petri dishes. Both culture vessels are regularly used to investigate cellular mechanisms after ultrasound application. The present study set out to explore differences in cellular responses in different culture systems as a result of ultrasound application using the same transducer.

Laser vibrometry is commonly used as a non-contact measure of the vibration displacement of the surfaces of ultrasonic devices (Xiao et al. 2016). Laser vibrometer measurements of the Duoson anterior face revealed an inherent variation in the vibration pattern of the transducer, where the inner edge of the transducer vibrated at a higher amplitude than the outer edge. This may be due to the convex shape of the plastic anterior cover of the transducer. The vibration displacement at the center of the device was close to zero, most likely because only the ring-shaped vibrating mass of the Duoson's 45-kHz transducer element was being driven, and not the 1-MHz transducer in the central nib. This ring shape could be seen in the spatial maps of vibration in Figure 4 and in the measured $p-$ values at 3 mm from the anterior face in Figure 8c. As the ultrasound intensity increased from 10 to 75 mW/cm^2, the average vibrational amplitude across the entire surface of the transducer increased by 127% as a consequence of driving the transducer at higher excitation levels.

Ultrasound wave propagation within the culture platforms was investigated using FEA. Standing waves existed in both in the 6-well plate and the Petri dish. Although the vibration response in the Petri dish presented a symmetric mode, the 6-well plate mode was non-symmetric. As a result, the cells present in different regions of the 6-well plate and the dish will have experienced different ultrasound waves intensities and peak pressure amplitudes. Additionally, vibrations were not limited to single wells of a 6-well plate where the transducer was placed, but the entire well plate was predicted to vibrate. Moreover, the FEA results confirmed that there was uneven distribution of the vibration displacement and pressure field, not only at the anterior face of the transducer, but also propagated to the bases of the culture platforms. Even though the attenuation of the displacement amplitude at the transducer anterior face is larger when in contact with water in the 6-well plate than in the Petri dish, as a result of the higher electrical impedance illustrated in Figure 5c, the displacement amplitude at the bottom surface of the well in the 6-well plate in which the ultrasound was directly applied is higher than in the Petri dish, as seen in Figure 7 (b, c). Together, these observations strongly indicate that the same transducer is capable of inducing different vibrations, and hence different pressure fields, in different cell culture platforms. The presence of standing waves, as a result of reflected waves in the confined space of the well-plate cultural platform, as well as the transmission of vibration between wells (in the case of the 6-well plate), makes it difficult to correlate the ultrasound intensity and vibrational amplitudes generated by the transducer with the ultrasound dose experienced by the cells seeded at the base of the culture systems.

Simulations also illustrated that at the same ultrasound intensity there was higher maximum pressure and vibrational displacement amplitude, both with higher standard deviations, across the base in 6-well plates compared with Petri dishes. Therefore, it was likely that the cells on the base experienced more extensive motion in 6-well plate than in Petri dish and, hence, may have been more prone to detachment or damage in 6-well plates upon ultrasound application. This might explain the lower mean metabolic activities observed in 6-well plates than in 35-mm dishes at the higher intensities of 25 and 75 mW/cm^2 and also the absence of mineralized matrix in certain regions of the 6-well plates after 9 days of exposure to an ultrasound intensity of 10 mW/cm^2.

The FEA-predicted pressure field in a Petri dish was compared with pressure measurements in the tank. The predicted peak negative pressure in the Petri dishes at Mode I ranged from 15- 39 kPa across the central 20-mm diameter of the well, compared with 20−29 kPa measured peak-negative pressure at 5 mm beneath the transducer over the same diameter, amounting to a 25%−34% difference. This further demonstrates that standard tank-based acoustic field characterization of ultrasound transducers poorly represents the pressure fields experienced in cell culture platforms such as Petri dishes. The beam width was wide compared with the dimensions of the culture wells as observed by Patel et al. (2015), who also found biological evidence of ultrasound transmission to other wells of a 6-well plate.

The FEA results in the present study bear a resemblance to those in the study by Leskinen and Hynynen (2012), who measured the pressure fields and vibration amplitudes of 6-well plates excited by a transducer positioned below the plate with a short water path between the anterior face and the well base. They found that the combination of reflections and Lamb wave plate vibrations induced by the ultrasonic excitation resulted in uncertainties of up to 700% in ultrasound exposure conditions. Leskinen and Hynynen's study was conducted at higher frequencies (650 kHz to 10 MHz), where the reflection coefficient and consequently the reflection amplitudes of the water-polystyrene interface would be higher than at 45 kHz. However, the standard deviations of RMS vibration displacement in Table 2

suggested a variance of 110%−120% (with 95% confidence) in the vibration experienced by the cell layer in the 6-well plate and a variance of 58%−80% variance in the Petri dish, which are still significant discrepancies. Thus, any controlled ultrasound exposure system must minimize seco ndary vibrations induced on the cell growth surface for accurate data interpretation.

The peak negative pressure 3 mm from the anterior front face of the transducer exhibited a ring-shaped beam pattern with another peak in the center of the beam (Fig. 8a−c). This is a common pattern in the near field of an ultrasonic device, where the arrival times from different areas of the anterior face (and spreading of the beam in this case) result in constructive and destructive interference and the positions of maxima and minima can change significantly with small changes in distance, as evidenced by the beam pattern at 5 mm (Fig. 8d−f), where the beam now has one central, smoothed peak. Therefore, experiments requiring a controlled ultrasound field should preferably be conducted in the far field to avoid the inherent unpredictability of the near field.

This study indicated that the Duoson device is not the ideal device to use in the investigation of biological effects *in vitro,* and instead, custom-designed devices tailored to the desired outcomes of the *in vitro* trial should be used. If driven with a signal generator and power amplifier, these devices would have the added advantage of allowing investigation of several variations of pulse characteristics, amplitudes and even frequency. Once the optimal *in vitro* conditions are known, the same conditions could be carefully reproduced *in vivo* to test for healing effects. Hensel et al. (2011) investigated the ultrasound wave propagation in cell culture wells using simulations that were verified by hydrophone measurements and determined the acoustic parameters of the materials used for culture plates and growth medium. They also reported the presence of standing waves and ring interference patterns caused by reflections at interfaces, causing local maximal pressure amplitude to increase by a factor of 5. Additionally, minor variations in culture medium volumes (as low as 2.56%) could increase or decrease the peak rarefaction pressure at a cell layer by a factor of 2, which may significantly affect the cells.

This work shows that the experimental setup results in the presence of standing waves, consequently leading to uncontrolled exposure of the cells to ultrasound. Despite the presence of standing waves is inherent in experimental setups involving Petri dishes and multiwell plates, the literature has many examples of studies of biological effects on cells where their presence is not appreciated and their influence is not considered. The other weakness in such experiments is the lack of calibration of the acoustic field. There is a wish among biological researchers to use either Petri dishes or multiwell plates as they are standard containers for growing cells and allow the growth environment to be fully controlled, but they do not allow for control of the ultrasound field or, therefore, the ultrasound dose to which the cells are exposed. There may be a benefit in using a 35-mm dish over multiwell plates as ultrasound will not be transmitted from one experimental replicate to another. Nevertheless, it was found that as ultrasound intensity increased, the cell attachment efficiency decreased because the ultrasound energy was being concentrated in the container, leading to higher levels of exposure. This was evidenced by a nearly 75% reduction in metabolic activity per well as well as poor focal adhesion, both indicating poor cell survival, in the case of cells treated with 75 mW/cm^2 ultrasound intensity. Cell cycle analysis and TEM images confirmed the formation of cell debris, possibly cells bursting under high energy and mitochondrial damage as well as endoplasmic reticulum swelling following ultrasound exposure. Previously, Sura et al. (2001) determined that continuous ultrasound waves (generated using a 25-kHz magnetostrictive transducer and TFI-1 chisel-shaped tip, with tip displacement set at 9.84, 12.23 or 18.20 μm, over a period of 30 s) caused rat osteoblasts to detach and lose viability whether the cells were in suspension or attached to the Petri dish in the period 0−20 h after exposure. It is also known that ultrasound causes mitochondrial dysfunction and autophagy in nasopharyngeal carcinoma cells (Li et al. 2018) and mitochondrial enlargement in ovarian cancer cells (Xiang et al. 2014). Recently, Wang et al. (2019) used microarray data from NCBI GEO Dataset databases to perform mining analysis, which indicated that low-intensity ultrasound activated different cell death transcription factors (299 death regulators) in cancerous or non-cancerous cells (total of 13 different cell types) and changed the redox status of the cells, known to be linked to mitochondrial damage (Pelicano et al. 2004). Wu et al. (2018) also suggested that cavitation induced with low-frequency ultrasound could trigger endoplasmic reticulum stress, downregulating the PI3K/AKT/mTOR signalling pathway in prostate cancer cells. To validate these effects, it is critical that experimental apparatus and schemes used to investigate the effects of ultrasound application on cells are optimized such that the frequencies and intensities capable of delivering therapeutic effect in bone repair and regeneration can ultimately be identified. The recommendation is to avoid experimental setups that lead to standing wave formation in the container and poor acoustic field calibration. To understand what cells are experiencing when exposed to ultrasound, the ideal container would be acoustically transparent, the ultrasound field would be well characterized and the ultrasound dose would be well controlled and measurable.

CONCLUSIONS

This study explored the propagation of continuous wave ultrasound in two different and widely used cell culture platforms, namely, multiwell (6-well) plates and Petri dishes with the same well diameter. The ultrasound waves produced by the same transducer at the same resonant frequency and intensity, for the same exposure time, propagated not just differently in these culture platforms but also led to different biological effects in terms of Saos-2 cell metabolic activity and calcium deposition. The base of 6-well plates vibrated at a higher amplitude and experienced higher acoustic pressure in an asymmetrical fashion than that measured in Petri dishes, and this may have been responsible for increased cell detachment and death in this system. Mitochondrial rupture and endoplasmic reticulum swelling were the main features of dying cells after treatment with ultrasound at higher intensities in 35-mm dishes. Due to the confined space of both culture wares relative to the wavelength of the ultrasound, standing waves were generated in both set-ups, and in the case of 6-well plates, ultrasound was not just limited to the well where the transducer was placed but was predicted to propagate across the entire plate. Thus, it can be concluded that characterization of acoustics in different culture systems is critical in the interpretation of experimental results as it contributes to determining the cell fate, which may be applicable not only to bone cells but also to other cells linked to neuropathy, angiogenesis, cementogenesis in tooth, and so on. Future work should focus on developing standardized cell culture systems that are reliable and reproducible to study the effects of ultrasound on cells such as for application in bone repair.

Acknowledgments—This work is funded by the Engineering and Physical Sciences Research Council and part of the Ultrasurge Project under Grant EP/R045291/1. We thank Dr. Yao Jiang, School of Biomedical Sciences, University of Birmingham for assisting with flow cytometry.

Conflict of interest disclosure—The authors report no potential competing interests.

REFERENCES

Aliabouzar M, Lee SJ, Zhou X, Zhang GL, Sarkar K. Effects of scaffold microstructure and low intensity pulsed ultrasound on chondrogenic differentiation of human mesenchymal stem cells. Biotechnol Bioeng 2018;115:495–506.

Angle SR, Sena K, Sumner DR, Virdi AS. Osteogenic differentiation of rat bone marrow stromal cells by various intensities of low-intensity pulsed ultrasound. Ultrasonics 2011;51:281–288.

Azuma Y, Ito M, Harada Y, Takagi H, Ohta T, Jingushi S. Low-intensity pulsed ultrasound accelerates rat femoral fracture healing by acting on the various cellular reactions in the fracture callus. J Bone Miner Res 2006;16:671–680.

Gao Q, Walmsley AD, Cooper PR, Scheven BA. Ultrasound stimulation of different dental stem cell populations: Role of mitogen-activated protein kinase signaling. J Endod 2016;42:425–431.

Gao Q, Cooper PR, Walmsley AD, Scheven BA. Role of piezo channels in ultrasound-stimulated dental stem cells. J Endod 2017;43:1130–1136.

Ghorayeb SR, Patel US, Walmsley AD, Scheven BA. Biophysical characterization of low-frequency ultrasound interaction with dental pulp stem cells. J Ther Ultrasound 2013;1:12.

Hasegawa T, Miwa M, Sakai Y, Niikura T, Kurosaka M, Komori T. Osteogenic activity of human fracture haematoma-derived progenitor cells is stimulated by low-intensity pulsed ultrasound in vitro. J Bone Joint Surg Br 2009;91:264–270.

Heckman JD, Ryaby JP, McCabe J, Frey JJ, Kilcoyne RF. Acceleration of tibial fracture-healing by non-invasive, low-intensity pulsed ultrasound. J Bone Joint Surg Am 1994;76:26–34.

Hensel K, Mienkina MP, Schmitz G. Analysis of ultrasound fields in cell culture wells for in vitro ultrasound therapy experiments. Ultrasound Med Biol 2011;37:2105–2115.

Huang W, Hasegawa T, Imai Y, Takeda D, Akashi M, Komori T. Low-intensity pulsed ultrasound enhances bone morphogenetic protein expression of human mandibular fracture haematoma-derived cells. Int J Oral Maxillofac Surg 2015;44:929–935.

Imai Y, Hasegawa T, Takeda D, Akashi M, Lee SY, Niikura T, Shibuya Y, Kurosaka M, Komori T. The osteogenic activity of human mandibular fracture haematoma-derived cells is stimulated by low-intensity pulsed ultrasound in vitro. Int J Oral Maxillofac Surg 2014;43:367–372.

Leskinen JJ, Hynynen K. Study of factors affecting the magnitude and nature of ultrasound exposure with in vitro set-ups. Ultrasound Med Biol 2012;38:777–794.

Li J, Zhang Q, Ren C, Wu X, Zhang Y, Bai X, Lin Y, LI M, Fu J, Kopylov P, Wang S, Yu T, Wang N, Xu C, Zhanga Y, Yang B. Low-intensity pulsed ultrasound prevents the oxidative stress induced endothelial-mesenchymal transition in human aortic endothelial cells. Cell Physiol Biochem 2018;45:1350–1365.

Lim K, Kim J, Seonwoo H, Park SH, Choung PH, Chung JH. In vitro effects of low-intensity pulsed ultrasound stimulation on the osteogenic differentiation of human alveolar bone-derived mesenchymal stem cells for tooth tissue engineering. Biomed Res Int 2013;2013 269724.

Maddi A, Hai HK, Ong ST, Sharp L, Harris M, Meghji S. Long wave ultrasound may enhance bone regeneration by altering OPG/RANKL ratio in human osteoblast-like cells. Bone 2006;39:283–288.

Man J, Shelton RM, Cooper PR, Landini G, Scheven BA. Low intensity ultrasound stimulates osteoblast migration at different frequencies. J Bone Miner Metab 2012a;30:602–607.

Man J, Shelton RM, Cooper PR, Scheven BA. Low-intensity low-frequency ultrasound promotes proliferation and differentiation of odontoblast-like cells. J Endod 2012b;38:608–613.

McCormick SM, Saini V, Yazicioglu Y, Demou ZN, Royston TJ. Interdependence of pulsed ultrasound and shear stress effects on cell morphology and gene expression interdependence of pulsed ultrasound and shear stress effects on cell morphology and gene expression. Ann Biomed Eng 2006;34:436–445.

Naruse K, Miyauchi A, Itoman M, Mikuni-Takagaki Y. Distinct anabolic response of osteoblast to low-intensity pulsed ultrasound. J Bone Miner Res 2003;18:360–369.

National Institute for Health and Care Excellence (NICE). EXOGEN ultrasound bone healing system for long bone fractures with non-union or delayed healing. 2019. Available at: https://www.nice.org.uk/guidance/mtg12. Accessed October 01, 2021.

Padilla F, Puts R, Vico L, Raum K. Stimulation of bone repair with ultrasound: A review of the possible mechanic effects. Ultrasonics 2014;54:1125–1145.

Patel US, Ghorayeb SR, Yamashita Y, Atanda F, Walmsley AD, Scheven BA. Ultrasound field characterization and bioeffects in multiwell culture plates. J Ther Ultrasound 2015;3:1–13.

Pelicano H, Carney D, Huang P. ROS stress in cancer cells and therapeutic implications. Drug Resist Updat 2004;7:97–110.

Reher P, Elbeshir ENI, Harvey W, Meghji S, Harris M. The stimulation of bone formation in vitro by therapeutic ultrasound. Ultrasound Med Biol 1997;23:1251–1258.

Reher P, Doan N, Bradnock B, Meghji S, Harris M. Therapeutic ultrasound for osteoradionecrosis: An in vitro comparison between 1 MHz and 45 KHz machines. Eur J Cancer 1998;34:1962–1968.

Sant'Anna EF, Leven RM, Virdi AS, Sumner DR. Effect of low intensity pulsed ultrasound and BMP-2 on rat bone marrow stromal cell gene expression. J Orthop Res 2005;23:646–652.

Scheven BA, Millard JL, Cooper PR, Lea SC, Walmsley AD, Smith AJ. Short-term in vitro effects of low frequency ultrasound on odontoblast-like cells. Ultrasound Med Biol 2007;33:1475–1482.

Scheven BA, Man J, Millard JL, Cooper PR, Lea SC, Walmsley AD, Smith AJ. VEGF and odontoblast-like cells: Stimulation by low frequency ultrasound. Arch Oral Biol 2009;54:185–191.

Sena K, Angle SR, Kanaji A, Aher C, Karwo DG, Sumner DR, Virdi AS. Low-intensity pulsed ultrasound (LIPUS) and cell-to-cell communication in bone marrow stromal cells. Ultrasonics 2011;51:639–644.

Sun JS, Hong RC, Chang WHS, Chen LT, Lin FH, Liu HC. In vitro effects of low-intensity ultrasound stimulation on the bone cells. J Biomed Mater Res 2001;57:449–456.

Sura H, Shelton RM, Walmsley AD. Osteoblast viability and detachment following exposure to ultrasound in vitro. J Mater Sci Mater Med 2001;12:997–1000.

Uddin SM, Qin YX. Enhancement of osteogenic differentiation and proliferation in human mesenchymal stem cells by a modified low intensity ultrasound stimulation under simulated microgravity. PLoS One 2013;8:e73914.

Wang J, Lai B, Nanayakkara G, Yang Q, Sun Y, Lu Y, Shao Y, Yu D, Yang WY, Cueto R, Fu H, Zeng H, Shen W, Wu S, Zhang C, Liu Y, Choi ET, Wang H, Yang X. Experimental data-mining analyses reveal new roles of low-intensity ultrasound in differentiating cell death regulatome in cancer and non-cancer cells via potential modulation of chromatin long-range interactions. Front Oncol 2019;9:600.

Wu Y, Liu X, Qin Z, Hu L, Wang X. Low-frequency ultrasound enhances chemotherapy sensitivity and induces autophagy in PTX-resistant PC-3 cells via the endoplasmic reticulum stress-mediated PI3K/Akt/mTOR signaling pathway. Onco Targets Ther 2018;11:5621–5630.

Xiang J, Leung AW, Xu C. Effect of ultrasound sonication on clonogenic survival and mitochondria of ovarian cancer cells in the presence of methylene blue. J Ultrasound Med 2014;33:1755–1761.

Xiao D, Fan Q, Xu C, Zhang X. Measurement methods of ultrasonic transducer sensitivity. Ultrasonics 2016;68:150–154.

Young MJR, Bradnock BRDP. Apparatus for ultrasonic therapeutic treatment. US Patent: US 6565520 B1, 2003.

Yue Y, Yang X, Wei X, Chen J, Fu N, Fu Y, Ba K, Li G, Yao Y, Liang C, Zhang J, Cai X, Wang M. Osteogenic differentiation of adipose-derived stem cells prompted by low-intensity pulsed ultrasound. Cell Prolif 2013;46:320–327.